

Available online at www.sciencedirect.com

jmr&t
Journal of Materials Research and Technology
journal homepage: www.elsevier.com/locate/jmrt



Original Article

Experimental and numerical analyses of residual stress redistributions in large steel dies: Influence of tempering cycles and rough milling



Morteza Sadeghifar^a, Mahshad Javidikia^{a,*},
Abdelhalim Loucif^b, Mohammad Jahazi^a, Victor Songmene^a

^a Department of Mechanical Engineering, École de Technologie Supérieure, Montreal, QC H3C 1K3, Canada

^b Finkl Steel-Sorel, St-Joseph-de-Sorel, QC J3R 3M8, Canada

ARTICLE INFO

Article history:

Received 25 December 2022

Accepted 6 March 2023

Available online 10 March 2023

Keywords:

Rough milling

Tempering

Quenching

Residual stresses

3D finite element model

P20 mold steel

ABSTRACT

The aim of the present research was to study the residual stress variations induced by heat treatment and rough milling operations of large forged steel blocks. The heat treatment process includes quenching and tempering operations. An efficient strategy based on a size sensitivity analysis (SSA) was proposed to reach the actual values of residual stresses in large-size steel blocks by using small-size workpieces in laboratory scale without damaging the blocks. The residual stresses were measured and compared after the first and second tempering and the rough milling. A 3D finite element (FE) model was developed to predict superficial residual stresses and was then calibrated experimentally. The results showed that the residual stresses after the first and second tempering were highly compressive on and near the surface. In addition, the resultants of the residual stresses after double tempering processes were almost equal. Therefore, the second tempering could be omitted from the manufacturing process. It was also found that both surface and sub-surface hoop and radial residual stresses were highly tensile after the rough milling. Finally, the 3D FE model can be used as a predictive tool to predict residual stresses for rough milling to avoid conducting expensive, time-consuming experimentations and measurements.

© 2023 The Authors. Published by Elsevier B.V. This is an open access article under the CC BY-NC-ND license (<http://creativecommons.org/licenses/by-nc-nd/4.0/>).

1. Introduction

Specialty steels are extensively used in critical components such as turbine shafts, aircraft landing gears, dies and molds, etc. [1]. Their manufacturing process often consists of casting in large size ingots followed by open die forging, quenching, tempering, and finally, machining [1,2], as shown in Fig. 1. Quenching and tempering (Q&T) heat treatments are two

important stages that result in significant microstructural changes affecting the geometrical integrity and mechanical properties of the final product [3].

The quenching process is applied after a forging operation to strengthen the material and improve the blocks' material properties [4,5]. However, distortion and residual stresses are produced due to cooling after the quenching process. The tempering process is carried out to decrease the distortion and residual stresses by heating the material [6]. The rough milling

* Corresponding author.

E-mail address: mahshad.javidikia.1@ens.etsmtl.ca (M. Javidikia).

<https://doi.org/10.1016/j.jmrt.2023.03.044>

2238-7854/© 2023 The Authors. Published by Elsevier B.V. This is an open access article under the CC BY-NC-ND license (<http://creativecommons.org/licenses/by-nc-nd/4.0/>).

process is conducted as an intermediate stage for these large blocks before fine machining (finishing) or smooth polishing to create custom parts using rotary cutters. Rough milling is characterized by high temperature, large strain, and high strain rate, and therefore, it induces distortion in the subsurface layer and affects the distribution of residual stresses in the material, or at least in the subsurface layer. Hence, it is important to quantify the impact of the rough milling process on surface and subsurface residual stresses and optimize the rough milling process to achieve minimum subsurface damage and residual stresses.

Little data is available on the analysis of residual stresses in Q&T steel blocks, and in particular, in large size ones. Deng and Ju [7] examined the residual stresses after the quenching and tempering heat treatments of small API J55 steel. The comparison of residual stresses after quenching and tempering showed that the tempering process relaxed the residual stresses induced by the quenching process. Tong et al. [8] investigated the residual stresses after induction hardening and subsequent quenching and tempering of a small shaft part made of AISI 4140H steel. The results showed that the quenching-induced surface residual stress was compressive. It was also found that the residual stress decreased with increasing the tempering temperature.

Ding et al. [9] analyzed the evolution of the residual stresses during tempering of short specimens made of 700 L low-carbon micro-alloyed steel. They observed that after tempering at 300 °C for 30 min, the residual stress decreased from 487 MPa to 200 MPa, whereas after tempering at 600 °C for 30 min, the residual stress diminished to 174 MPa. Bouissa et al. [3] analyzed residual stresses after the water quenching process of large size forged steel blocks made of P20 mold steel using FEM. They found that the surface residual stresses were highly compressive, while the residual stresses at the rest of the block were tensile.

The residual stress distribution after milling operations was measured in several research works. Guo et al. [10] analyzed the residual stresses induced by the whirlwind milling of AISI 52100 Steel. The results showed that high compressive residual stresses were produced in steel specimens. Masmiahi and Sarhan [11] experimentally investigated residual stresses in inclined end milling of AISI 1050 Steel. They found that axial depth of cut and cutting speed had less impact on the residual stresses. Ma et al. [12] measured the peripheral residual stress after the end milling of AISI 4140 steel and investigated its correlation with thermo-mechanical loads. They reported that the thermal load in end milling created tensile surface residual stresses, whereas the mechanical load generated compressive surface residual stresses.

Finite element method has been used as an efficient tool to model machining processes and predict the residual stresses in orthogonal cutting [13] and turning operations [14]. There are some finite element (FE) studies that modeled a real

milling process in the 3D space by simulating a 2D orthogonal cutting process [15–19] by transforming milling tool geometry configuration to orthogonal cutting [20]. Only a small number of works on 3D FE modeling of milling-induced residual stresses was found in the literature. Jiang et al. [21] predicted the residual stresses generated during high-speed circular milling of AA 7050-T7451 using a 3D FE model in the AdvantEdge™ software and then experimentally validated the simulated stresses. They reported that the distribution of residual stresses was affected by uncut chip thickness and the cutting sequence (up or down milling). Feng et al. [22] developed a FE model to predict the residual stresses induced by the milling of Inconel 718 using DEFORM® software. They found that an increase in axial depth of cut hardened the workpiece with larger compressive residual stresses, whereas an increment in feed rate raised the temperature in the shear zone, which led to higher tensile residual stresses.

The above review of the literature shows that few studies were carried out to obtain and compare the residual stresses in small (lab-scale) workpieces after quenching-tempering processes and subsequent milling operations. Despite the vast applications of the milling process, no published research analysis on the simulation of residual stresses induced by rough milling processes was found. In addition, no strategy for measuring the residual stresses in large-size components such as large blocks was presented by the previous research studies.

In the present project, first, a new efficient strategy based on a SSA was designed to capture the actual residual stresses in large steel blocks by employing small-size workpieces in laboratory scale without having to ruin the large blocks. This was because the experimental measurements of the residual stresses on the blocks after both quenching-tempering and milling processes were impossible due to the large size and high cost of the blocks. Then, the residual stresses induced by the first and second tempering of the large blocks were measured experimentally based on the SSA strategy. In addition, the residual stresses induced by the dry rough milling of the large blocks were measured experimentally based on SSA and predicted numerically using finite element method (FEM).

2. Materials and experimental methods

In the present study, the rough milling operations were carried out on 127 mm × 127 mm × 25.4 mm (5 in × 5 in × 1 in) rectangular blocks. The samples were saw cut from large forged blocks with the initial dimensions of 1071 mm × 1080 mm × 2705 mm (42.15 in × 42.5 in × 106.5 in). The material was made of a medium carbon low alloy steel, similar in composition to a P20 grade, which was provided by Finkl Steel-Sorel, as displayed in Fig. 2. After casting and forging operations, the large steel block went through water quenching, and then, one or two tempering operations were performed in a gas fired



Fig. 1 – The manufacturing process of large-size steels in Finkl Steel-Sorel.



Fig. 2 – The large steel block used in the study.

furnace. The heat treatment process began with the austenitization below 900 °C for approximately 48 h. It was followed by the quenching process in water. The heat treatment ended with tempering at above 550 °C for around 48 h [3].

Rough milling operations were carried out using TiAlN and AlCrO coated tungsten carbide inserts (SDES1906MPR-IN4005). A 177.8-mm (7-in) Face Mill 5G5M-70R10 was used as a toolholder (Fig. 3). The tool geometry includes Side Cutting Edge Angle (SCEA) or Lead Angle, Bake Rake Angle (BRA), and Side Rake Angle (SRA) equal to +12°, +10°, and +5°, respectively. The milling parameters are listed in Table 1.

To ensure that the experimental determination of the residual stresses is valid due to the large size of the blocks, a size sensitivity analysis was carried out. In fact, for the size of a rough milled sample, there can be a threshold value above which the residual stresses do not approximately change with the size, as shown in Fig. 4. Accordingly, the residual stresses of the sample of this threshold size should be equal to those of the large blocks. The samples' shape and dimensions are displayed in Fig. 5.

During the tempering process, an oxide layer always forms at the sample's surfaces. In order to measure the residual stresses in the samples (workpieces), the oxide layer should be removed. As a result, the two samples after the 1st tempering

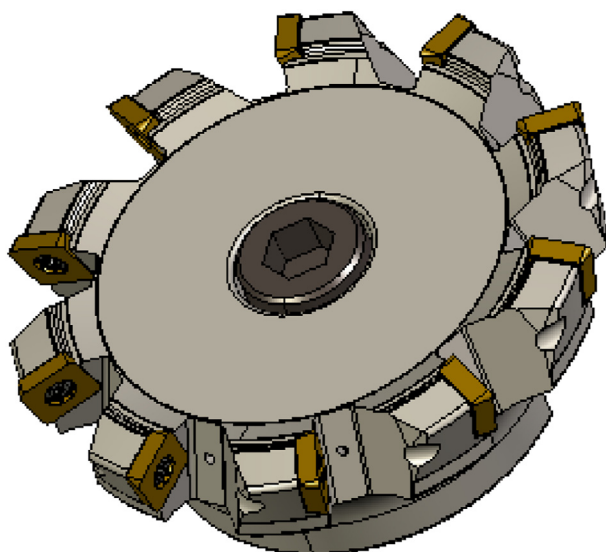


Fig. 3 – The milling toolholder and inserts [23].

Table 1 – Rough milling parameters.

Cutting speed V (m/min)	Feed rate per insert f (mm/rev)	Depth of cut D (mm)
159.2	1.319	2.54

and 2nd tempering were polished with a Silicon Carbide paper using a Metaserv 2000 Polisher. It needs mentioning that the polishing was conducted smoothly to avoid changing the residual stress distribution.

Residual stresses were measured based on X-Ray Diffraction (XRD) method using a Pulstec μ-X360n machine, which uses Debye-Scherrer ring image (based on a diffracted cone) and cos α method [24] to measure and calculate residual stresses (see Fig. 6(a)) [25,26]. The time required for measuring each point is about 2 min using the Pulstec machine. Residual stresses were measured at three points and then were averaged to reduce the impact of inhomogeneity in the material or accidental damage on the measured surface [27]. The X-ray diffraction constants and parameters are given in Table 2.

Residual stress profile measurements were conducted after material removal with a Struers LectroPol-5 electro-polishing machine (Fig. 6(b)). On a small (laboratory) scale, the saltwater electrolyte was pumped onto a small area of the workpiece's surface. A voltage of 32 V was then applied for a set time determined based on the required removal depth. When current was applied, the electrolyte acted as a conductor and allowed the current to flow from the anode to the cathode. Therefore, the workpiece surface was oxidized and dissolved in the electrolyte solution [28]. Consequently, metal ions were removed from the workpiece and moved into the cathode according to Faraday's first law, which expressed that the mass of the removed metal is proportional to the applied current and the exposure time [29].

The depth of the removed material (P-profile) was measured using a Mitutoyo SJ-400 profilometer (Fig. 6(c)). In this contact-type instrument, the stylus' tip touches the sample surface and measures the vertical positions of the surface's points to obtain the removed depth [28].

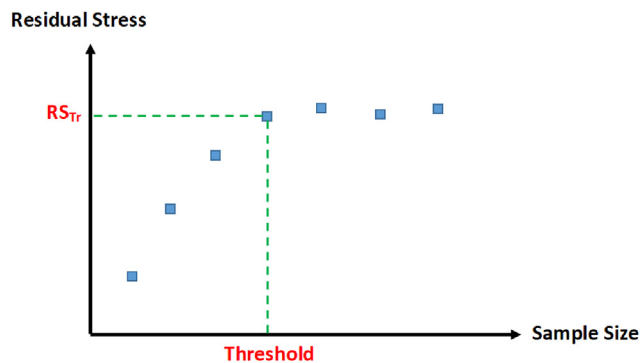


Fig. 4 – Determination of the sample's threshold size using the size sensitivity analysis.

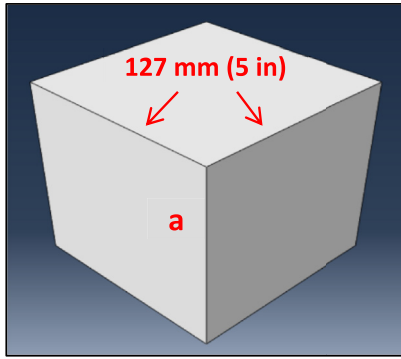


Fig. 5 – The samples' shape and dimensions for the SSA.

Sample No.	Size "a" mm (in)
1	25.4 (1)
2	50.8 (2)
3	76.2 (3)
4	101.6 (4)

3. Results and discussion

3.1. Size sensitivity analysis

Cubic blocks with the side dimensions of 127 mm (5 in) were used for the size sensitivity analysis of residual stress measurements. The measurements were done for four heights: 25.4, 50.8, 76.2, and 101.6 mm (1, 2, 3, and 4 in). The superficial hoop and radial residual stresses were measured at the center of the sample's surface. The variation of the residual stresses with the sample's height is shown in Fig. 7. As seen in this figure, the residual stresses remained almost constant with the variation of the sample's height after a height of 25.4 mm,

showing that the residual stresses of the large blocks are equal to those of the sample of 25.4-mm height.

3.2. Residual stresses after the first tempering

As seen in Fig. 8, the superficial hoop and radial residual stresses were -548 and -345 MPa, respectively. In addition, both hoop and radial residual stresses were compressive on and near the surface, and then, increased to small tensile values at the depth of around $44 \mu\text{m}$ and remained almost constant after this depth. This profile showed the balancing effect of the compressive and tensile residual stresses. It was also observed that the hoop and radial residual stresses were different only on the surface, whereas they showed

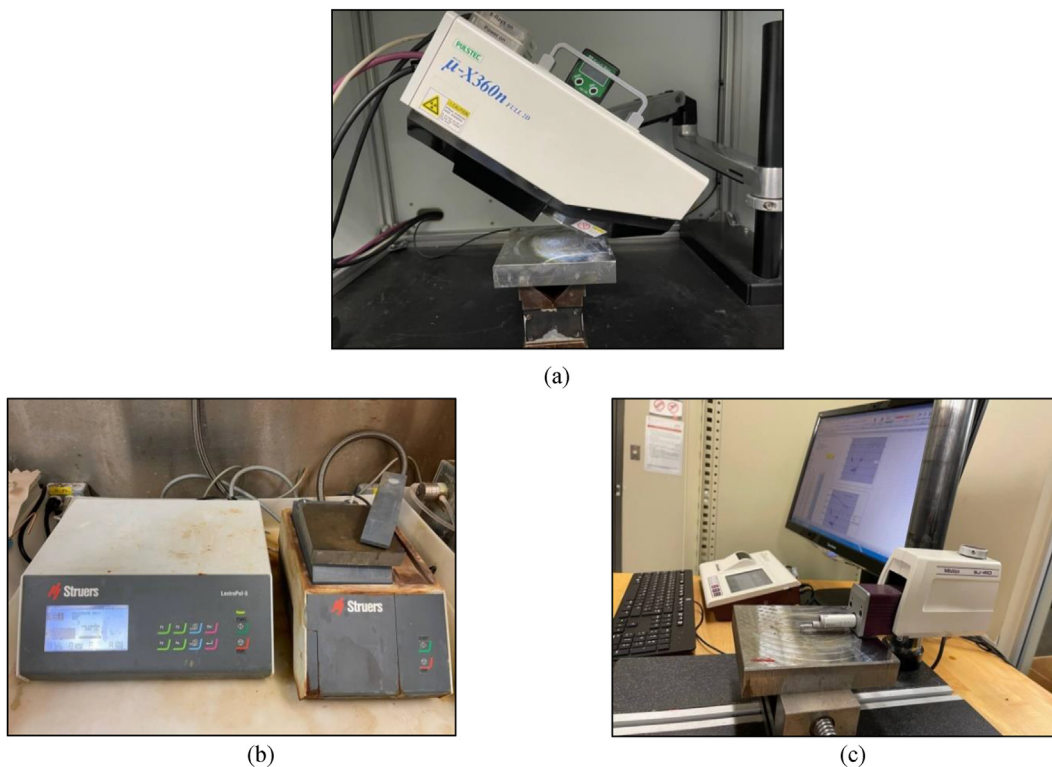


Fig. 6 – (a) Residual stress measurements using a Pulstec μ -X360n machine, (b) material removal with a Struers LectroPol-5 electropolishing machine, and (c) depth measurements of the removed material with a Mitutoyo SJ-400 profilometer.

Table 2 – Constants and parameters for residual stress measurements using a Pulstec machine.

Material	P20 Steel (bcc)	Voltage	30 kV
hkl plane	{211}	Current	1 mA
Bragg angle	156.41°	X-Ray incidence angle	35°
D-spacing	0.117021 nm	X-Ray irradiation time	30 s
Tube	Cr_K α	Aperture	1 mm
Wavelength	0.2291 nm	Working distance	39 mm

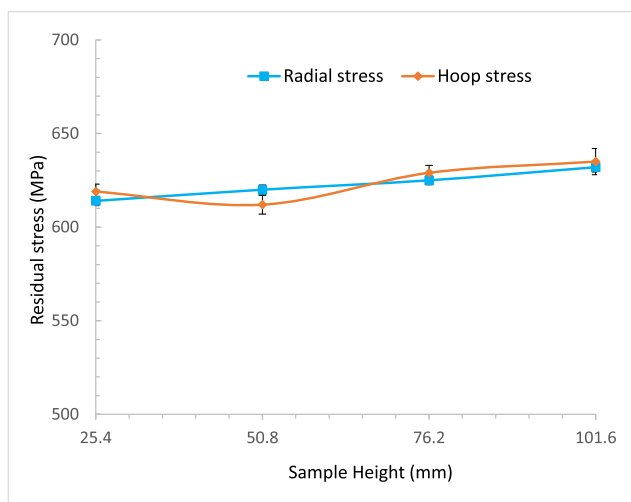


Fig. 7 – The variation of residual stresses with the sample's height in hoop and radial directions.

almost the same values and trends on the subsurface of the sample.

It must be mentioned that the residual stresses measured at this step were induced by both the quenching and tempering processes (assuming that residual stresses induced during forging were all released during the very long austenitization treatment at about 900 °C). The compressive character of the residual stresses are attributed to the fact that the intensive water quenching process generated a martensitic

phase in the surface and near surface regions of the work-piece, leading to high hardness and compressive residual stresses, as also reported by other researchers [3,30].

3.3. Residual stresses after the second tempering

The hoop and radial residual stresses on the surface were equal to -338 and -494 MPa, respectively, as displayed in Fig. 9. Moreover, similar to the residual stresses after the first tempering, both surface and near-surface hoop and radial residual stresses were highly compressive, and then, increased to small tensile or compressive values at a depth of around 23 μ m and almost did not change thereafter. It is also seen that the hoop and radial residual stresses were different only on the surface, while they exhibited almost similar trends under the surface of the sample.

It is important to note that, after the second tempering, the magnitudes of both hoop and radial residual stresses only changed very slightly compared to the first tempering and both residual stresses were still compressive and their compressive resultants were almost equal. Therefore, it could be concluded that the second tempering does not affect the character and magnitude of the residual stresses.

3.4. Residual stresses after the rough milling

Fig. 10 displays the plots of the variation of the hoop and radial residual stresses with the depth below the machined surface. As observed in this figure, both surface and sub-surface hoop and radial residual stresses were highly tensile and both were equal to 620 MPa. Furthermore, both residual stresses showed almost the same descending trend, where they diminished from the surface to the depth of the sample. However, the radial stress reached a stress level close to that of the bulk material at a depth of 70 μ m, which was earlier than the hoop stress reaching the steady-state condition at 120 μ m. It is also observed that the magnitude and character of superficial residual stresses' significantly changed from compressive (-494 MPa) after the second tempering process to tensile (+622 MPa) after the rough milling process. This demonstrated that the rough milling process considerably affected the residual

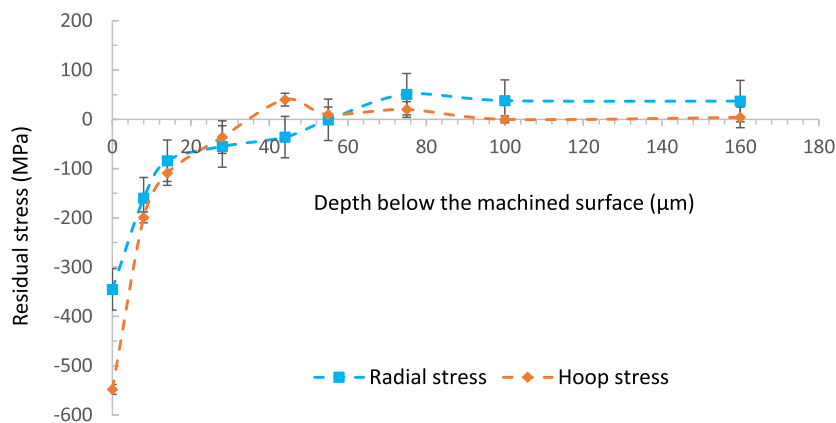


Fig. 8 – Residual stress profiles in hoop and radial directions after the first tempering.

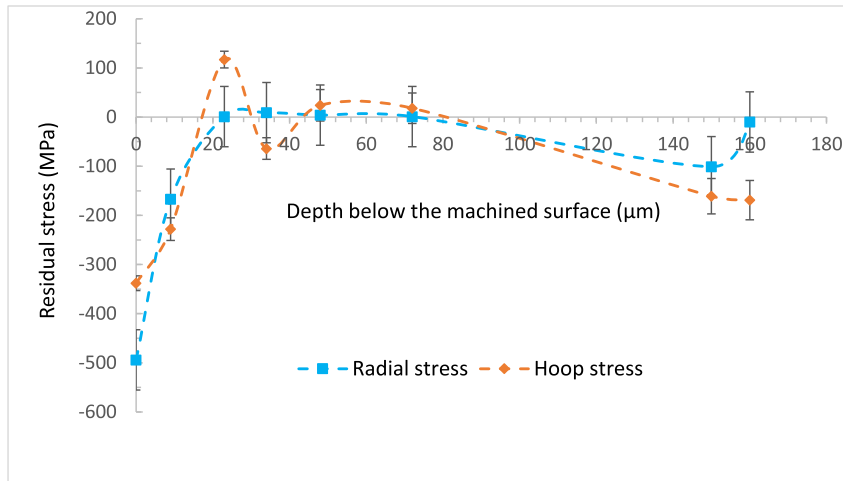


Fig. 9 – Residual stress profiles in hoop and radial directions after the second tempering.

stresses. It is important to mention that the rough milling process is followed by subsequent finishing machining and/or smooth polishing operations that remove 150–300 µm, leading to the removal of the 120-µm tensile layer. Therefore, the residual stresses in the final products are always very small (less than ±100 MPa).

In a rough milling process, high feed rate and depth of cut cause large tool-chip contact area and frictional heat, leading to high temperature and residual stresses. In contrast, high feed rate and depth of cut augment material removal rate ($MRR, V \times f \times D$), resulting in greater heat evacuation by the chip from the workpiece, and therefore, smaller temperature and residual stresses [24,31,32]. Therefore, in a milling process, the magnitude of the residual stresses depends significantly on the competition between these two phenomena [32–34]. In the present milling process, which is a rough milling with high values of feed rate and depth of cut, the first mechanism appeared dominating the second one, yielding tensile residual stresses. It needs mentioning that since the surface was rather rough after the dry rough milling, the standard deviation of the measured surface residual stresses

was relatively large at some points. This observation was in agreement with that reported by Ref. [12].

3.5. 3D finite element modeling of the rough milling process

In the present study, a 3D finite element model was developed to simulate the rough milling process of P20 Mold Steel using the DEFORM® software. The large block before the rough milling, the FE model to conduct the rough milling process, and the large block after the rough milling are shown in Fig. 11(a)–(c), respectively. The FE analysis is based on an updated Lagrangian formulation and implicit integration method.

The equations of motion during the rough milling process are expressed as [35,36]:

$$[M]\{\ddot{U}\} + \{R_{int}\} = \{R_{ext}\} \tag{1}$$

where $[M]$ is the mass matrix, $\{\ddot{U}\}$ is the acceleration vector ($\{U\}$ is the displacement), and $\{R_{int}\}$ and $\{R_{ext}\}$ are the vectors

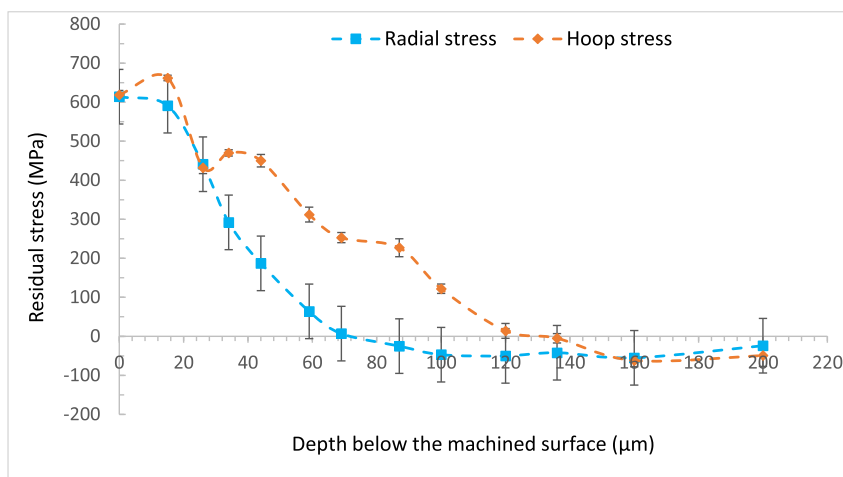


Fig. 10 – Residual stress profiles in hoop and radial directions after the rough milling.

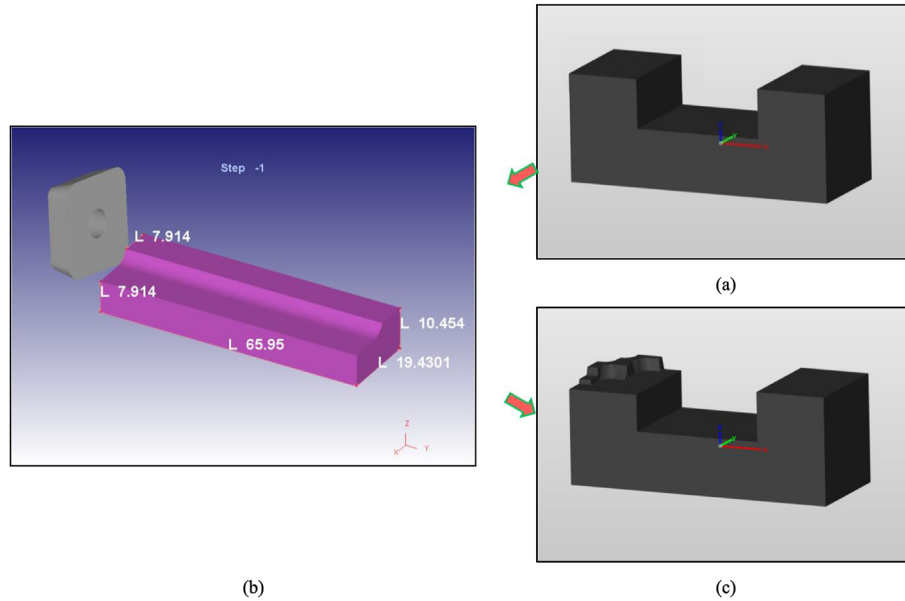


Fig. 11 – (a) The large block before the rough milling, (b) the FE model to conduct the rough milling process, and (c) the large block after the rough milling.

of internal and external forces, respectively. Moreover, $\{R_{int}\}$ equals:

$$\{R_{int}\} = [C_d]\{\dot{U}\} + [K_s]\{U\} \quad (2)$$

in which $[C_d]$ and $[K_s]$ are the damping and stiffness matrices, respectively. $\{R_{ext}\}$ contains the external forces applied during milling including the reaction forces at the supports.

Heat transfer during the milling process is formulated as [35,36]:

$$[C_T]\{\dot{T}\} + [K_T]\{T\} = \{\dot{Q}_g\} \quad (3)$$

where $[C_T]$ and $[K_T]$ are the volumetric heat capacitance and thermal conduction matrices, respectively. $\{\dot{Q}_g\}$ is also the total heat generation in the milling process.

The thermal contact between the tool and workpiece was assigned using the heat transfer through the tool-chip contact faces during the milling process as follows:

$$Q = h_{int} (T_{wp} - T_t) \quad (4)$$

where h_{int} is heat transfer coefficient, T_{wp} and T_t are the workpiece and tool's temperature at the tool-chip interface. A heat transfer coefficient of $10^5 \text{ W/m}^2\text{°C}$ was used for modeling and an initial temperature of 20 °C (room temperature) was considered for both tool and workpiece. It should be noted that the heat transfer coefficient was obtained through calibration when the steady-state condition for milling temperature was reached. The high value was assigned because the high pressure of the chip on the tool rake faces makes a perfect contact between the tool and chip. Another reason was to quickly reach the steady-state condition so as to shorten the milling simulation time and avoid excessive distortion of elements. Finally, the convection heat transfer that occurs between the workpiece surface and the environment (room) is described as:

$$Q = h (T_{wp} - T_{room}) \quad (5)$$

in which h is convection heat transfer coefficient, and $T_{room}(\text{°C})$ is the room temperature.

The Johnson-Cook constitutive equation was used for modeling thermo-visco-plastic deformation of the workpiece material as follows:

$$\sigma_{fl} = [A + B(\epsilon)^n] \left[1 + C \ln\left(\frac{\dot{\epsilon}}{\dot{\epsilon}_0}\right) \right] \left[1 - \left(\frac{T - T_{room}}{T_{melt} - T_{room}}\right)^m \right] \quad (6)$$

where σ_{fl} is the flow stress of the workpiece material, ϵ is the plastic strain, $\dot{\epsilon}$ the plastic strain rate (s^{-1}), $\dot{\epsilon}_0$ the reference plastic strain rate (s^{-1}), $T(\text{°C})$ the workpiece temperature, and $T_{melt}(\text{°C})$ the melting temperature of the workpiece. Furthermore, A (MPa) is the initial yield strength, B (MPa) the hardening modulus, C the strain rate sensitivity coefficient, n the hardening coefficient, and m the thermal softening coefficient. The Johnson-Cook constants for a steel with similar composition to the one used in the present study is given in Table 3.

The mechanical contact between the tool and the workpiece was modeled using the shear friction model as follows:

$$\tau = m_f \tau_{Chip} \quad (7)$$

where m_f is the shear friction factor and τ_{Chip} is the shear flow stress in the chip at the tool-chip interface. The shear friction model was calibrated by comparing and matching the predicted residual stresses with the corresponding measurements.

Table 3 – The constants for the Johnson-Cook constitutive model for P20 mold steel [36–38].

A (MPa)	B (MPa)	n	C	m	$\dot{\epsilon}_0$ (1/s)	T_{melt} (°C)	T_{room} (°C)
145	565.6	0.154	0.03	1.8	1	1480	20

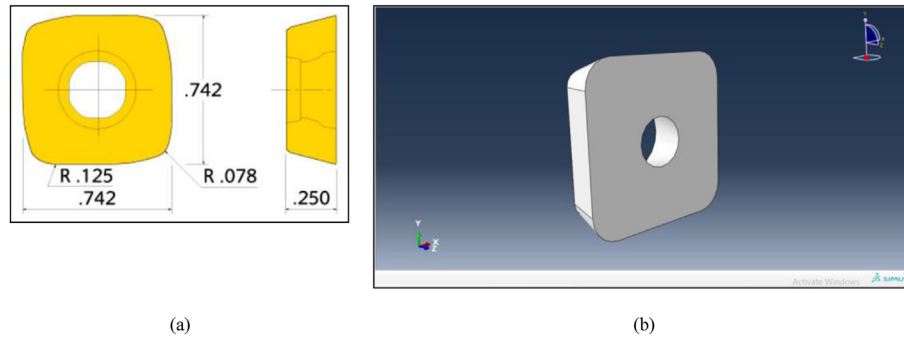


Fig. 12 – (a) The geometry of the insert SDES1906MPR-IN4005 [39] and (b) the insert part created with the STEP format using the Abaqus® software.

Table 4 – The mechanical, thermal, and material properties of the workpiece and tool [36–38].

Properties	P20 Steel	Tungsten Carbide	TiAlN coating
Density ρ (kg/m ³)	7850	11,900	5220
Young's modulus E (GPa)	E(T)	612	440
Poisson's ratio ν	0.3	0.22	0.23
Thermal conductivity k(W/m°C)	418.68 [0.065 + (0.10241–0.065)(1.0033–11.095 × 10 ⁻⁴) (T - 273)]	86	12
Specific heat capacity cJ/kg°C	420 + 0.504 T	337	15
Thermal expansion coefficient α (1/°C)	α (T)	4.9 × 10 ⁻⁶	9.2 × 10 ⁻⁶

For the developed FE model, the workpiece with a thermo-elasto-visco-plastic behavior was meshed with 60,000 tetrahedral elements. Insert SDES1906MPR-IN4005 (Fig. 12(a)) was first created with the STEP format in the Abaqus® software (Fig. 12(b)) and was then imported with the STL format into the DEFORM® software. The tool material was modeled as a rigid body and was meshed with 35,000 tetrahedral elements. The mechanical, thermal, and material properties of the carbide insert and TiAlN coating were adapted from Ref. [38]. The properties of AlCrO coating are not available in the literature. According to the literature, the total coating thickness of “TiAlN + AlCrO” is 2 μ m [40,41].

Since the coating thickness is very small, AlCrO coating can be neglected in the simulations. Mesh windows were applied to the workpiece and the tool in order to have a high-quality fine mesh in the milled workpiece and the tool tip. The workpiece and tool's material properties are provided in Tables 4–6.

Residual stresses were obtained after applying two steps: the rough milling process and the stress relaxation process. In

the first step, milling was conducted to reach the steady-state condition where milling characteristics including temperature remain almost constant with time. During the stress relaxation step, the tool was retracted and the mechanical boundary conditions (BCs) $V_x = V_y = V_z = 0$ were removed from the side faces of the workpiece in order to allow the workpiece material to relax by cooling down to room temperature. This cooling process was performed using a convection heat transfer to the workpiece and the chip. The mechanical and thermal boundary conditions for the milling and the stress relaxation steps in the FE model are shown in Fig. 13(a) and (b), respectively.

The modeling of cutting and residual stress steps took about 22 and 6 h using a computer system of Intel® Xeon® CPU E3-1225 V5 with a CPU speed of 3.30 GHz and a memory RAM of 64.0 GB. The variations of milling forces and temperature with time during the cutting process were monitored and the simulation runs were stopped when the steady state conditions for the forces and temperature were reached. In

Table 5 – Young's modulus in terms of temperature [38].

Temperature T (°C)	Young's modulus E(GPa)
20	210
150	192
260	180
344	191
427	188
482	186
538	157
650	114
1371	69

Table 6 – Thermal expansion coefficient in terms of temperature [38].

Temperature T (°C)	Thermal expansion coefficient α (1/°C)
20	1.17 × 10 ⁻⁵
94	1.21 × 10 ⁻⁵
205	1.23 × 10 ⁻⁵
316	1.24 × 10 ⁻⁵
427	1.30 × 10 ⁻⁵
482	1.31 × 10 ⁻⁵
816	1.35 × 10 ⁻⁵
1371	1.39 × 10 ⁻⁵

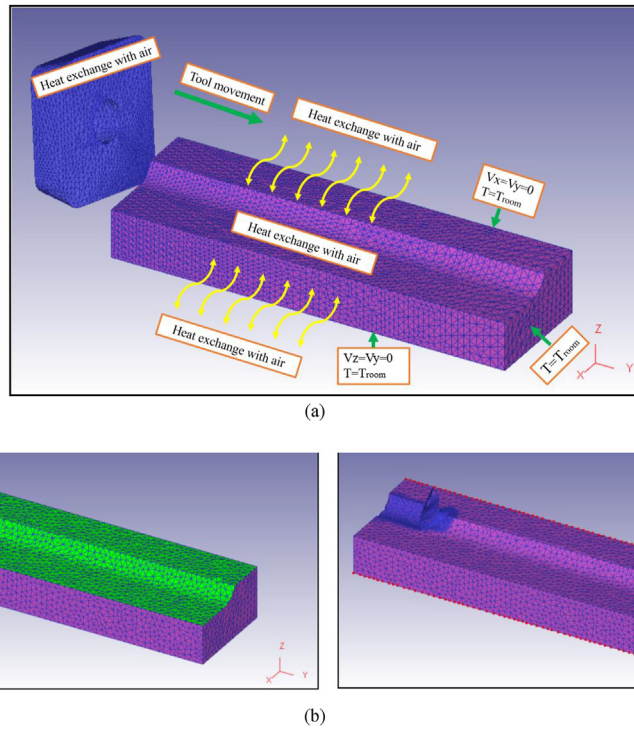


Fig. 13 – Thermal and mechanical boundary conditions in (a) the rough milling step and (b) the stress relaxation step.

addition, the dimensions of the workpiece were chosen large enough to be far from the boundaries of the workpiece in order to eliminate the effects of the boundary conditions on the cutting and residual stress processes.

3.6. Calibration of the 3D FE model with the experiment

Fig. 14 provides an illustrative example of the rough milling process simulation results using the DEFORM® software. The results show that the maximum cutting temperature occurred at the chip root. The developed 3D FE model was calibrated by comparing the predicted hoop and radial superficial residual stresses with the corresponding experimental ones for the parameters listed in Table 7. It needs mentioning that the experimentally measured residual stresses after the 2nd

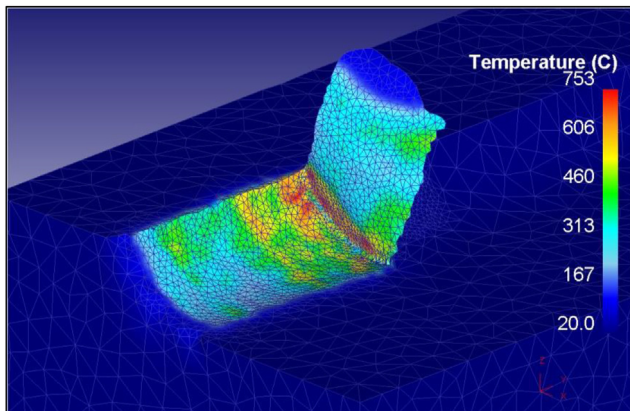


Fig. 14 – The predicted temperature in the rough milling process simulated using the DEFORM® software.

tempering were applied to the FE model as the pre stresses in the simulation of the rough milling process. Since the feed rate and depth of cut had high values in the rough milling, it was not possible to measure the machining forces due to limitations in the capacity of the dynamometer.

Fig. 15(a) and (b) show the simulated residual stresses in the hoop and radial directions. It needs mentioning that the residual stresses were obtained by averaging the residual stress values of the elements near the chip root. This is because the stress values are not maintained by DEFORM® software during simulations when the cutting is going on for a large cutting length. This was also reported by the other research works [42–45]. As displayed in Fig. 16, the percentage error between the measured and predicted residual stresses in the hoop and radial directions are 11.8 and 1.3%, respectively. This shows that there is good agreement between the predicted and measured residual stresses. The predicted and measured residual stresses were well matched by exploring different values of shear friction factor and heat transfer coefficient and choosing appropriate coefficients by calibrating the simulation results with the experimentation ones. The calibrated values are given in Table 8.

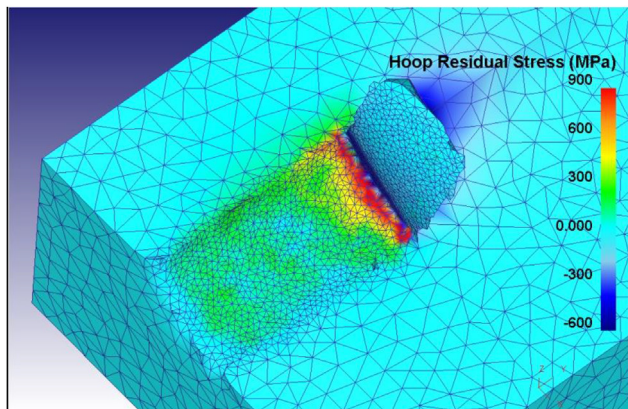
It needs to be mentioned that the errors originate from making the following assumptions and simplifications [13]:

Table 7 – The milling parameters and tool geometry for the calibration test.

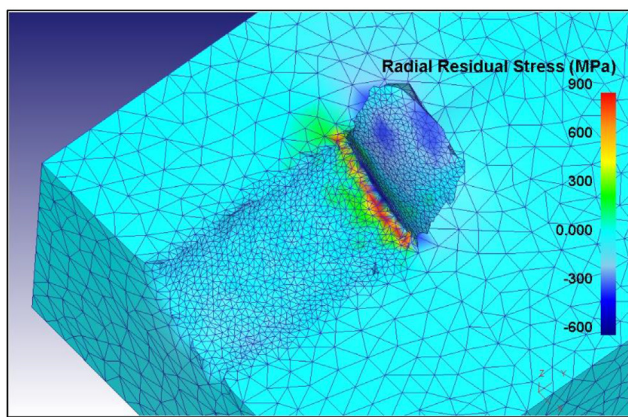
V (m/min)	f (mm/rev)	D (mm)	SCEA (deg)	BRA (deg)	SRA (deg)
159.2	1.319	2.54	+12	+10	+5

Table 8 – The calibrated frictional and thermal coefficients in the FE model.

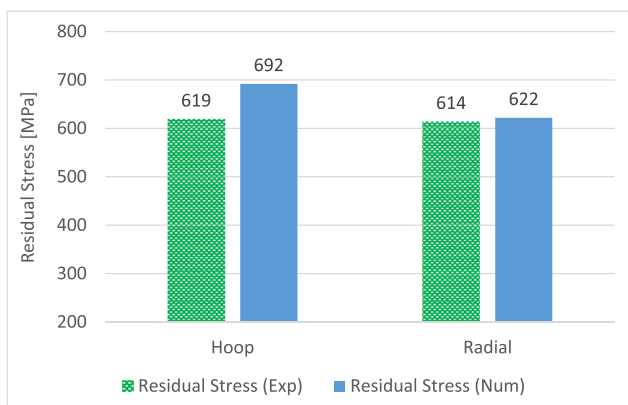
Shear Friction Factor	0.35
Heat Transfer Coefficient [kW / (m ² °C)]	10 ⁵
Heat Convection Coefficient [kW / (m ² °C)]	0.02



(a)



(b)

Fig. 15 – The simulated residual stresses in (a) hoop and (b) radial directions.**Fig. 16 – The comparison of the measured and predicted residual stresses for the rough milling process.**

From a geometrical viewpoint, for simplicity, only a portion of the workpiece was modeled with a relatively short length. However, this length was large enough to reach the steady-state conditions during the cutting process. Moreover, the friction coefficient in the experiments was a function of chip sliding velocity, contact pressure, and contact temperature at the tool-chip-workpiece interface, whereas this coefficient was considered as a constant value in the simulations as it was not easy to identify the variable friction coefficient experimentally. Also, the thermal conductance at the tool-chip interface was in terms of the gap, contact temperature, and contact pressure in the experiments, while it was assumed to be a constant value in the simulations for simplifications. Lastly, tool wear which causes a change in the tool geometry was neglected during the simulations, while it occurred in the experiments.

4. Summary and conclusions

In the present research study, the residual stress analysis of large size forged steel blocks undergoing a manufacturing process consisting of ingot casting, open die forging, quenching, two tempering, and rough milling was carried out. An effective strategy based on a size sensitivity analysis was applied to obtain the actual residual stresses in the large-size steel blocks by using small-size workpieces without needing for destructing the large blocks. The residual stress distributions were experimentally obtained and compared after the first tempering, the second tempering, and the rough milling processes. It was found that the surface and near-surface hoop and radial residual stresses after the first and second tempering were highly compressive. Moreover, the resultants of the residual stresses after the two tempering were almost the same. The experimental results also showed that both hoop and radial residual stresses were highly tensile on and near the surface after the rough milling process. It was observed that the superficial residual stresses shifted from large compressive values after the second tempering operation to large tensile values after the rough milling operation. The tensile residual stresses produced as a result of the rough milling process are present in a thickness of about 120 μm below the surface and are expected to be eliminated by subsequent finishing and smooth polishing processes. Furthermore, the superficial residual stresses were simulated using a developed 3D finite element model in the DEFORM® software. This FE model can be used in the machining industry to simulate the residual stresses for different milling parameters instead of doing a large number of costly, time-consuming experimental milling tests and residual stress measurements.

Declaration of competing interest

The authors declare that they have no known competing financial interests or personal relationships that could have appeared to influence the work reported in this paper.

Acknowledgments

The authors would like to thank Finkl Steel-Sorel for funding this research study, supplying workpiece materials, inserts,

and tool holders, and preparing the samples. The authors also acknowledge MITACS for financially supporting this research work through Grant No. IT17671.

REFERENCES

- [1] Talebi SH, Jahazi M, Melkonyan H. Retained austenite decomposition and carbide precipitation during isothermal tempering of a medium-carbon low-alloy bainitic steel. *Materials* 2018;11(8):1441.
- [2] Talebi SH, Ghasemi-Nanasa H, Jahazi M, Melkonyan H. Influence of starting microstructure on dilatation behavior during tempering of a high strength steel. *Mater Sci Forum* 2018;941:305–10. Trans Tech Publications Ltd.
- [3] Bouissa Y, Bohlooli N, Shahriari D, Champliaud H, Morin JB, Jahazi M. FEM modeling and experimental validation of quench-induced distortions of large size steel forgings. *J Manuf Process* 2020;58:592–605.
- [4] Bouissa Y, Zorgani M, Shahriari D, Champliaud H, Morin JB, Jahazi M. Microstructure-based FEM modeling of phase transformation during quenching of large-size steel forgings. *Metall Mater Trans A* 2021;52(5):1883–900.
- [5] Lyassami M, Shahriari D, Ben Fredj E, Morin JB, Jahazi M. Numerical simulation of water quenching of large size steel forgings: effects of macrosegregation and grain size on phase distribution. *J Manuf Mater Process* 2018;2(2):34.
- [6] Talebi SH, Ghasemi-Nanasa H, Jahazi M, Melkonyan H. In situ study of phase transformations during non-isothermal tempering of bainitic and martensitic microstructures. *Metals* 2017;7(9):346.
- [7] Deng X, Ju D. Modeling and simulation of quenching and tempering process in steels. *Phys Procedia* 2013;50:368–74.
- [8] Tong D, Gu J, Yang F. Numerical simulation on induction heat treatment process of a shaft part: involving induction hardening and tempering. *J Mater Process Technol* 2018;262:277–89.
- [9] Ding W, Liu Y, Xie J, Sun L, Liu T, Yuan F, Pan J. Effect of carbide precipitation on the evolution of residual stress during tempering. *Metals* 2019;9(6):709.
- [10] Guo Q, Chang L, Ye L, Wang Y, Feng H, Cao Y, Li Y. Residual stress, nanohardness, and microstructure changes in whirlwind milling of GCr15 steel. *Mater Manuf Process* 2013;28(10):1047–52.
- [11] Masmiaati N, Sarhan AA. Optimizing cutting parameters in inclined end milling for minimum surface residual stress-Taguchi approach. *Measurement* 2015;60:267–75.
- [12] Ma Y, Feng P, Zhang J, Wu Z, Yu D. Prediction of surface residual stress after end milling based on cutting force and temperature. *J Mater Process Technol* 2016;235:41–8.
- [13] Sadeghifar M, Sedaghati R, Jomaa W, Songmene V. A comprehensive review of finite element modeling of orthogonal machining process: chip formation and surface integrity predictions. *Int J Adv Manuf Technol* 2018;96(9):3747–91.
- [14] Javidikia M, Sadeghifar M, Songmene V, Jahazi M. 3D FE modeling and experimental analysis of residual stresses and machining characteristics induced by dry, MQL, and wet turning of AA6061-T6. *Mach Sci Technol* 2021;25(6):957–83.
- [15] Tang ZT, Liu ZQ, Pan YZ, Wan Y, Ai X. The influence of tool flank wear on residual stresses induced by milling aluminum alloy. *J Mater Process Technol* 2009;209(9):4502–8.
- [16] Li JL, Jing LL, Chen M. An FEM study on residual stresses induced by high-speed end-milling of hardened steel SKD11. *J Mater Process Technol* 2009;209(9):4515–20.
- [17] Salahshoor M, Guo YB. Finite element simulation and experimental validation of residual stresses in high speed dry milling of biodegradable magnesium–calcium alloys. *Int J Mech Sci* 2014;80:153–9.
- [18] Meng L, Khan AM, Zhang H, Fang C, He N. Research on surface residual stresses generated by milling Ti6Al4V alloy under different pre-stresses. *Int J Adv Manuf Technol* 2020;107(5):2597–608.
- [19] Yao G, Liu Z, Song Q, Wang B, Cai Y. Numerical prediction and experimental investigation of residual stresses in sequential milling of GH4169 considering initial stress effect. *Int J Adv Manuf Technol* 2022:1–14.
- [20] Feng Y, Hung TP, Lu YT, Lin YF, Hsu FC, Lin CF, Lu YC, Liang SY. Residual stress prediction in laser-assisted milling considering recrystallization effects. *Int J Adv Manuf Technol* 2019;102:393–402.
- [21] Jiang X, Li B, Yang J, Zuo X, Li K. An approach for analyzing and controlling residual stress generation during high-speed circular milling. *Int J Adv Manuf Technol* 2013;66(9):1439–48.
- [22] Feng Y, Pan Z, Lu X, Liang SY. Analytical and numerical predictions of machining-induced residual stress in milling of Inconel 718 considering dynamic recrystallization. vol. 51388. In: *International Manufacturing Science and Engineering Conference*. American Society of Mechanical Engineers; 2018, June, V004T03A023.
- [23] www.ingersoll-imc.com, February 15, 2022.
- [24] Sadeghifar M, Sedaghati R, Jomaa W, Songmene V. Finite element analysis and response surface method for robust multi-performance optimization of radial turning of hard 300M steel. *Int J Adv Manuf Technol* 2018;94(5):2457–74.
- [25] Sasaki T. New generation X-ray stress measurement using debye ring image data by two-dimensional detection. vol. 783. In: *Materials Science Forum*. Trans Tech Publications Ltd; 2014. p. 2103–8.
- [26] Lin J, Ma N, Lei Y, Murakawa H. Measurement of residual stress in arc welded lap joints by $\cos\alpha$ X-ray diffraction method. *J Mater Process Technol* 2017;243:387–94.
- [27] Feng Y, Hsu FC, Lu YT, Lin YF, Lin CT, Lin CF, Lu YC, Liang SY. Residual stress prediction in ultrasonic vibration-assisted milling. *Int J Adv Manuf Technol* 2019;104:2579–92.
- [28] Sadeghifar M. Development of the analysis and optimization strategies for prediction of residual stresses induced by turning processes. Doctoral Dissertation. Concordia University; 2017.
- [29] Fitzpatrick ME, Fry AT, Holdway P, Kandil FA, Shackleton J, Suominen L. Measurement good practice guide No. 52: determination of residual stresses by X-ray diffraction - issue 2. National Physical Laboratory; 2005.
- [30] Javidikia M, Sadeghifar M, Songmene V, Jahazi M. Low and high speed orthogonal cutting of AA6061-T6 under dry and flood-coolant modes: tool wear and residual stress measurements and predictions. *Materials* 2021;14(15):4293.
- [31] Pawade RS, Joshi SS, Brahmankar PK. Effect of machining parameters and cutting edge geometry on surface integrity of high-speed turned Inconel 718. *Int J Mach Tool Manufact* 2008;48(1):15–28.
- [32] Javidikia M, Sadeghifar M, Songmene V, Jahazi M. Effect of turning environments and parameters on surface integrity of AA6061-T6: experimental analysis, predictive modeling, and multi-criteria optimization. *Int J Adv Manuf Technol* 2020;110(9):2669–83.
- [33] Sadeghifar M, Javidikia M, Songmene V, Jahazi M. A comparative analysis of chip shape, residual stresses, and surface roughness in minimum-quantity-lubrication turning with various flow rates. *Int J Adv Manuf Technol* 2022;121:3977–87.

- [34] Javidikia M, Sadeghifar M, Songmene V, Jahazi M. On the impacts of tool geometry and cutting conditions in straight turning of aluminum alloys 6061-T6: an experimentally validated numerical study. *Int J Adv Manuf Technol* 2020;106(9):4547–65.
- [35] Sadeghifar M, Javidikia M, Songmene V, Jahazi M. Finite element simulation-based predictive regression modeling and optimum solution for grain size in machining of Ti6Al4V alloy: influence of tool geometry and cutting conditions. *Simulat Model Pract Theor* 2020;104:102141.
- [36] Shatla M, Kerk C, Altan T. Process modeling in machining. Part I: determination of flow stress data. *Int J Mach Tool Manufact* 2001;41(10):1511–34.
- [37] Tang DW, Wang CY, Hu YN, Song YX. Finite-element simulation of conventional and high-speed peripheral milling of hardened mold steel. *Metall Mater Trans* 2009;40(13):3245.
- [38] DEFORM® user's manual, Version 10.2.
- [39] <https://www.ramstaronline.net/catalogue/product/488717>, February 15, 2022.
- [40] Mkaddem A, Soussia AB, El Mansori M. Wear resistance of CVD and PVD multilayer coatings when dry cutting fiber reinforced polymers (FRP). *Wear* 2013;302(1–2):946–54.
- [41] Mkaddem A, Zeramdini B, El Mansori M, Mezlini S. Evaluation of tribothermal effectiveness of TiAlN-based bilayer coatings in cutting fiber-reinforced polymers. *Tribol Int* 2016;103:176–86.
- [42] Attanasio A, Ceretti E, Giardini C. 3D FE modelling of superficial residual stresses in turning operations. *Mach Sci Technol* 2009;13(3):317–37.
- [43] Attanasio A, Ceretti E, Cappellini C, Giardini C. Residual stress prediction by means of 3D FEM simulation. vol. 223. In: *Advanced Materials Research*. Trans Tech Publications Ltd; 2011. p. 431–8.
- [44] Proudian J. Simulating residual stress in machining; from post process measurement to pre-process predictions. Master dissertation. KTH Royal Institute of Technology; 2012.
- [45] Torrano I, Barbero O, Kortabarria A, Arrazola PJ. Prediction of residual stresses in turning of Inconel 718, vol. 223. *Trans Tech Publications Ltd*; 2011. p. 421–30.